engineering proceedings

MDPI

Proceeding Paper

The Influence of MIM Metamaterial Absorbers on the Thermal and Electro-Optical Characteristics of Uncooled CMOS-SOI-MEMS Infrared Sensors †

Moshe Avraham *, Mikhail Klinov and Yael Nemirovsky

Electrical and Computer Engineering Department, Technion—Israel Institute of Technology, Haifa 32000, Israel; mikhail.kl@campus.technion.ac.il (M.K.) ; nemirov@ee.technion.ac.il (Y.N.);

* Correspondence: smoa@campus.technion.ac.il

† Presented at The 11th International Electronic Conference on Sensors and Applications (ECSA-11), 26–28 November 2024; Available online: https://sciforum.net/event/ecsa-11.

Abstract: Uncooled infrared (IR) sensors including bolometers, thermopiles, and pyroelectrics have traditionally dominated the market. Nevertheless, a new innovative technology, dubbed TMOS sensor, has emerged. It is based on CMOS-SOI-MEMS (complementary-metal-oxide-semiconductor silicon-on-insulator micro-electromechanical systems) fabrication. This pioneering technology utilizes a suspended, micro-machined thermally insulated transistor to directly convert absorbed infrared radiation into an electrical signal. The miniaturization of IR sensors, including the TMOS, is crucial for seamless integration into wearable and mobile technologies. However, this presents a significant challenge: balancing size reduction with sensor sensitivity. Smaller sensor footprints can often lead to decreased signal capture and consequently, diminished performance. Metamaterial advancements offer a promising solution to this challenge. These engineered materials exhibit unique electromagnetic properties that can potentially boost sensor sensitivity while enabling miniaturization. Strategic integration of metamaterials into sensor design offers a pathway towards compact, high-sensitivity IR systems with diverse applications. This study explores the impact of electro-optical metal-insulator-metal (MIM) metamaterial absorbers on the thermal and electro-optical characteristics of CMOS-SOI-MEMS sensors in the mid-IR region. We target key thermal properties critical to IR sensor performance: thermal conductance (Gth), thermal capacitance (Cth), and thermal time constant (τth). The study shows how material selection, layer thickness, and metamaterial geometry fill-factor affect the sensor's thermal performance. An analytical thermal model is employed alongside 3D finite element software for precise numerical simulations.

Keywords: infrared; IR; sensor; CMOS; thermal; metamaterial; absorber; SOI; MEMS; finite-element-analysis; thermal; FDTD

Citation: Avraham, M.; Klinov, M.; Nemirovsky, Y. The Influence of MIM Metamaterial Absorbers on the Thermal and Electro-Optical Characteristics of Uncooled CMOS-SOI-MEMS Infrared Sensors. *Eng. Proc.* **2024**, *5*, x. https://doi.org/10.3390/xxxxx

Academic Editor(s):

Published: 26 November 2024

1. Introduction

Thermal infrared (IR) sensors have gained widespread adoption in diverse fields, including automotive, Internet of Things (IoT), intrusion detection systems, and smart building management (lighting/heating/temperature sensing) and wearable devices. This trend is expected to continue with a growing market forecast [1].

Commercially available uncooled IR technologies primarily rely on bolometers, thermopiles, and pyroelectric sensors [2]. However, recent advancements have introduced a new generation of uncooled thermal sensors based on CMOS-SOI-MEMS (complementary-metal-oxide-semiconductor silicon-on-insulator micro-electromechanical systems) technology, termed "TMOS" [3].

TMOS is a MEMS device featuring a suspended, thermally isolated, micro-machined floating transistor that absorbs infrared radiation. The resulting temperature change is

converted into an electrical signal. Operating in the subthreshold regime, TMOS offers significant advantages such as low power consumption (micro-Watts) and high temperature sensitivity. Figure 1 illustrates the TMOS schematically.

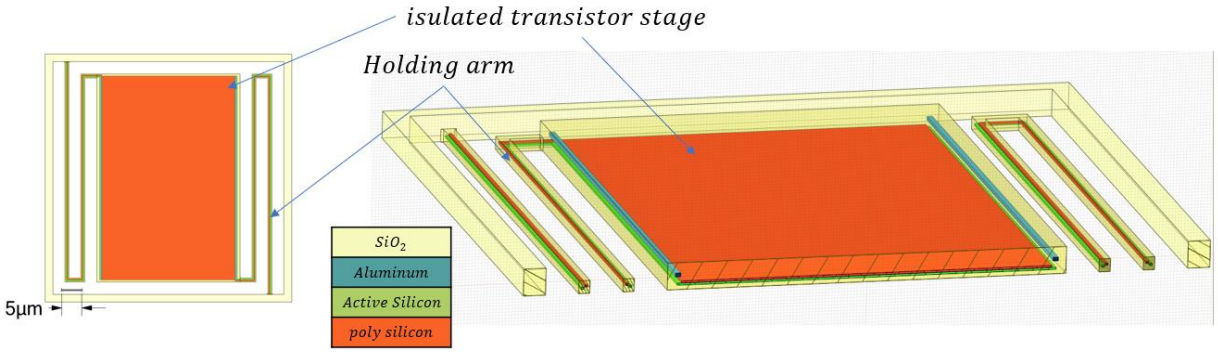

Figure 1. Schematic geometry of the TMOS: (**a**) Top view; (**b**) Cross section view of the geometry.

The miniaturization of infrared (IR) sensors has emerged as a critical aspect of their ongoing evolution, driven by the increasing demand for their integration into modern technologies like wearable electronics, mobile applications, optical gas sensing and biosensing [4,5]. Achieving this without compromising sensitivity presents a significant challenge, as shrinking size can often lead to diminished signal capture and performance.

However, recent advancements in metamaterial fabrication and design offer a promising solution to this conundrum. Metamaterials are artificially constructed structures engineered to exhibit electromagnetic properties unattainable in naturally occurring materials [6]. Meta-absorbers are a specific class designed to optimize absorption of incident electromagnetic radiation. These novel materials possess unique electro-magnetic properties that can potentially enhance sensor sensitivity while simultaneously enabling reductions in sensor size [7]. By strategically incorporating metamaterials into IR sensor architectures, researchers are paving the way for the development of a new generation of compact and highly sensitive IR systems with applications across diverse fields.

This work builds upon the investigation of thermal performance in Wafer-Level-Packaged (WLP) TMOS devices, as reported in [8,9]. The key thermal properties influencing the performance of infrared thermal sensors, including TMOS devices, are thermal conductivity (denoted by *Gth)*, thermal capacitance (denoted by *Cth*), and thermal time constant (denoted by τ_{th}). The present study focuses on the thermal performance of an integrated metamaterial absorber within a CMOS-SOI-MEMS thermal infrared sensor. Electromagnetic simulations of the metal-insulator-metal absorbers and TMOS performance were conducted using commercial Finite-Difference-Time-Domain (FDTD) software. We investigate the impact of material selection, layer thickness, and metamaterial geometry fill-factor on the sensor's thermal behavior. An analytical thermal model is employed alongside 3D finite element software for accurate numerical simulations.

2. Design and Methodology

2.1. MIM Meta-Absorber Design

MIM meta-absorbers consist of a thin dielectric layer sandwiched between two metal layers, with the top layer patterned into sub-wavelength size structures such as squares, circles, or other shapes. A MIM example with the top layer patterned into sub-wavelength disks is illustrated in Figure 2.

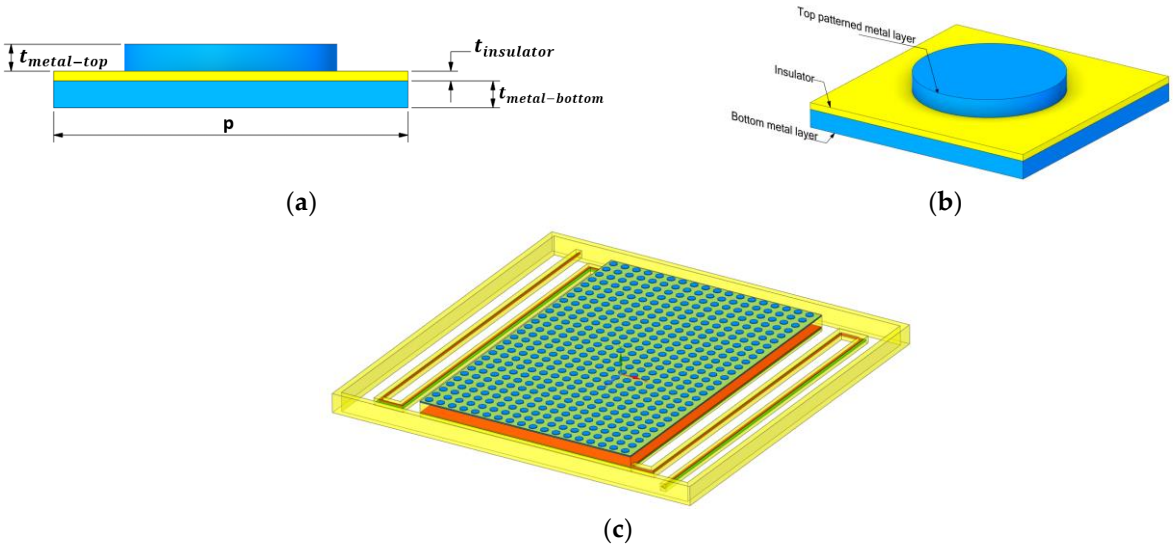

Figure 2. Schematic geometry of the MIM: (**a**) Side view; (**b**) 3-Dimensional view of the MIM geometry; (**c**) 3-Dimensional schematic illustration of the TMOS with MIM absorber.

The patterned top metal layer interacts with incident radiation, supporting localized surface plasmon resonances that concentrate the electromagnetic field within the dielectric layer.

2.2. Integration Approach with CMOS

The uniqueness of the TMOS is that all process of the fabrication is done in standard CMOS-SOI-MEMS fabrication facilities. The goal is to design and manufacture CMOS-compatible metamaterial absorber. Hence, the constrains of the standard CMOS and MEMS fabrication limitations must be addressed. For example, novel metamaterial absorber often uses Au (gold) and Ag (silver), due to the naturally high conductivity. However, gold and silver are not suitable for CMOS-fabrication due to high diffusivity, and expensive. Therefore, other metals need to be considered when designing a CMOS-compatible metamaterial such as Al (aluminum), Cu (copper) or W (Tungsten) [10]. In addition, the thickness of the materials layers and patterns should be considered to fabricate the design in CMOS fabrication facilities.

2.3. Electromagnetic Simulation and Modelling Techniques

A three-dimensional FDTD simulation was conducted using Ansys Lumerical software [11] to model the MIM absorber. A plane wave source was employed to generate electromagnetic radiation spanning wavelengths from 2.5 μm to 14 μm. Periodic boundary conditions were applied to the lateral boundaries to simulate an infinite periodic structure. Perfectly matched layer (PML) boundary conditions were implemented at the top and the bottom of the FDTD region to absorb outgoing waves. To quantify the reflected and absorbed electromagnetic energy, a two-dimensional field monitor was positioned above the source. Figure 3 illustrates the FDTD model. The materials refractive indexes were taken from the software library based on Palik or CRC references.

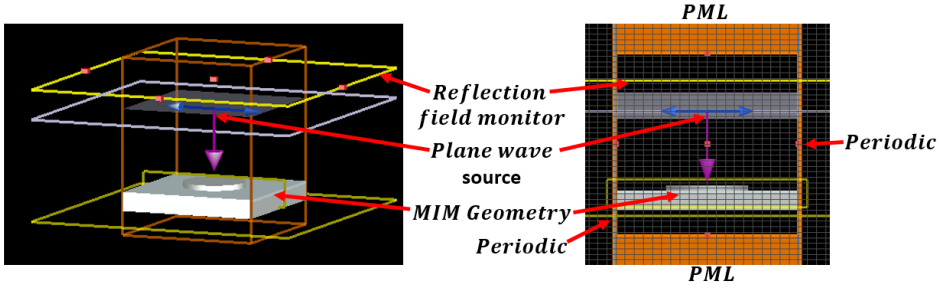

Figure 3. FDTD model illustration.

The reflected field and energy (R) were measured directly the power in the field monitor in Lumerical is normalized to the total power launched into the simulation. while the absorbed energy was calculated by subtracting the reflected energy from the incident energy. Given the presence of a bottom metal layer, transmission (T) was negligible and considered zero. Consequently, since the power injected to the power launched into the simulation is normalized the absorbed energy (A) could be determined using the energy conservation principle (the sum of the transmission, reflected and absorbed should be equal to the power injected to the simulation, knowing that the input power is normalized to 1):

$$A = 1 - R \tag{1}$$

2.4. Thermal Simulation and Modelling Techniques

The thermal modeling of the TMOS has been extensively discussed in previous publications [9,12]. This section provides a concise overview of the key components. The TMOS functions as a thermal infrared (IR) sensor by converting absorbed radiation power into an electrical signal. A thermally isolated sensor stage undergoes a temperature change due to the absorbed energy, which is then transduced into an electrical signal by the TMOS transistor. The conservation of energy dictates that the absorbed power within the device must be equivalent to the sum of the increase in stored power and the power dissipated or emitted. Hence the power balance equation is as follows:

$$P_{absorbed} = C_{th}\frac{d\Delta T(t)}{dt} + G_{th}\Delta T(t) \tag{2}$$

The absorbed optical power in the device is denoted by $P_{absorbed}$. Cth represents the thermal capacitance of the device, while Gth signifies its thermal conductance. ΔT denotes the time-dependent temperature change within the device. Given the deep vacuum packaging of the TMOS device (a few pascals, see [8]) and the dimensional disparity between the stage and the holding arms, the thermal conductance of the device is primarily determined by the thermal conductance of the holding arms (refer to Figure 1). The thermal conductance of the arms can be calculated using the following equation:

$$G_{th,arm} = \frac{k_{arm}A_{arm}}{L_{arm}} = \frac{1}{L_{arm}}\sum_{i=1}^{N} k_i A_i \tag{3}$$

The area through which heat flows is denoted by A_{arm}, while L_{arm} represents the arm length. The thermal conductivity of the material is given by k_i and the material area is given by A_i.

The thermal capacitance of the device is primarily influenced by the sensor stage, which houses the TMOS transistor. It can be calculated using the following equation:

$$C_{th} = \rho cV = \sum_{i=1}^{N} \rho_i c_i V_i \tag{4}$$

where the mass density of material i is represented by ρ_i, while c_i denotes its specific heat capacity. V_i signifies the volume of material i. The thermal and physical properties used in this work are presented in Table 1.

Table 1. Thermal and physical properties of CMOS-SOI compatible materials.

Parameter	Units	Aluminum	Silicon Dioxide	Silicon	Polycrystalline Silicon	Copper	Tungsten	Titanium
k—Thermal conductivity	$\frac{W}{m \times K}$	237	1.4	40	40	401	173	16.9
c—Specific heat capacity	$\frac{J}{kg \times K}$	900	730	700	700	385	134	520
ρ—Mass density	$\frac{Kg}{m^3}$	2700	2200	2329	2320	8960	19,300	4510

3. Results and Discussion

3.1. Electromagnetic Simulation Results

The electromagnetic energy absorption of the TMOS material layers was simulated using the FDTD method, as outlined in the design and methodology section. Initial simulations were conducted without the MIM absorber. Figure 4 illustrates the resulting electromagnetic absorption as a function of wavelength.

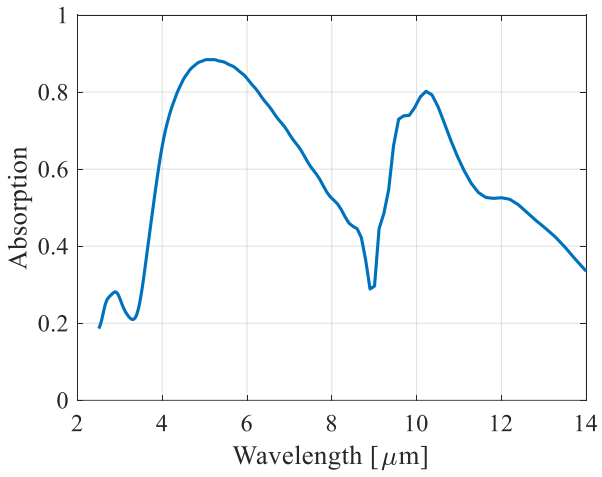

Figure 4. TMOS layers electromagnetic absorption as a function of the wavelength.

The absorption spectrum exhibited two prominent peaks centered at approximately 5 µm and 10 µm, with maximum absorption coefficients of 0.88 and 0.8, respectively. The average absorption across the examined band was approximately 0.5. While the non-uniform absorption profile and broad spectral features may limit the suitability of this material for direct application in Non-Dispersive Infrared (NDIR) gas sensing without additional optical filtering, the absorption efficiency could potentially be enhanced by at least 12% at the 5 µm wavelength and even more at other wavelengths through the integration of optical components.

Figure 5 illustrates the FDTD simulation results for a proposed integrated MIM structure with a periodic disk array as the top metal layer. The absorption spectrum of the MIM structure is shown as a function of wavelength and disk radius.

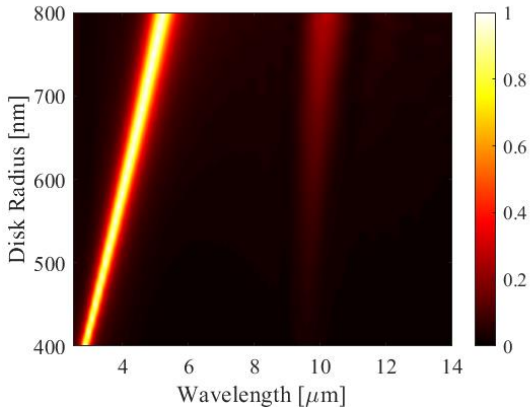

Figure 5. The MIM electromagnetic absorption as a function of wavelength and top metal disk radius. The simulation employed an aluminum top metal layer, a silicon dioxide insulator, and a bottom metal layer. The top metal layer was 100 nm, the insulator was 55 nm, and the bottom metal layer was 150 nm. The periodicity of the MIM is 1 μm. The color bar visually represents the fraction of absorbed energy.

The depicted figure illustrates near-perfect absorption (>98%) of single-frequency resonance in the mid-infrared region. As the disk radius increased, a discernible redshift in the peak resonance frequency was observed, accompanied by a corresponding decrease in the quality factor of the absorbance. This reduction in quality factor can be attributed to increased losses associated with larger disk radii. Additionally, the spectra reveal a secondary absorption peak centered around 10 microns, which is primarily due to the intrinsic absorption of silicon dioxide. As the disk radius grows, enhanced scattering and increased field interaction with the oxide contribute to a heightened absorption at this wavelength. However, given the relatively thin silicon dioxide layer, the secondary absorption remains relatively modest, approximately 10% at radius disk of 600 nm.

3.2. Thermal Simulation Results and Impact

Steady-state thermal simulations were conducted using a 3D FEA model in Ansys Mechanical software [13]. To assess the impact of the MIM structure on the pixel array. Boundary conditions consisted of a fixed temperature at the pixel frame and a heat load of 1μW applied to the pixel stage. The simulation outcomes are illustrated in Figure 6.

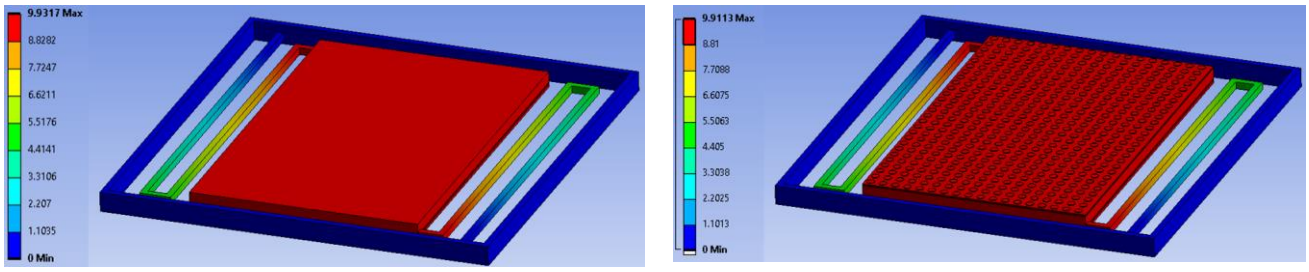

(**a**) (**b**)

Figure 6. Steady-State thermal simulation results of the temperature changes: (**a**) The TMOS without MIM; (**b**) TMOS with MIM.

The thermal conductance of the TMOS sensor, as calculated using Equation (2), was determined to be 1.0069×10^{-7} W/K and 1.0089×10^{-7} W/K for the configurations without and with the MIM structure, respectively. Analytical calculation using Equation (3) and properties from Table 1 yields 1.0012×10^{-7} W/K. The steady-state thermal simulation results demonstrate that the MIM structure exerts a negligible influence on the overall thermal conductance. This observation aligns with the theoretical predictions derived from

Equations (3) and (4). At steady state, the temperature differential within the device is primarily determined by the applied power load and the thermal conductance of the TMOS holding arms. As the MIM structure does not materially affect the thermal conductance of these arms, its impact on the steady-state thermal behavior is minimal.

While the MIM structure does not significantly affect the thermal conductance, it is expected to influence the thermal capacitance. Consequently, the thermal time constant which is a function of both conductance and capacitance $\tau = C_{th}/G_{th}$, should be impacted by the presence of the MIM structure. Figure 7 illustrates the transient simulation results comparing the thermal response with and without the MIM structure.

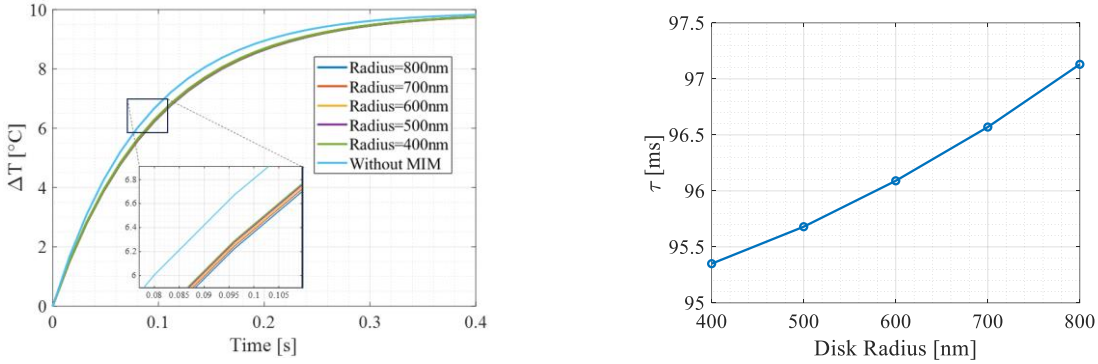

(**a**) (**b**)

Figure 7. Transient thermal simulation results: (**a**) The TMOS temperature difference as a function of the time, with and without the MIM structure; (**b**) Thermal time constant results from the transient simulation as function of the disk radius. Without the MIM structure the thermal time constant of the TMOS is 86 ms.

As depicted in Figure 7, the radius of the MIM structure exerts a small influence on the thermal time constant of the TMOS. Specifically, an increase in the MIM radius leads to a slightly corresponding rise in the thermal time constant. Furthermore, it is intriguing to investigate the potential impact of the MIM metal on this thermal behavior. Figure 8 presents transient thermal simulations conducted with various CMOS-compatible metals to address this question.

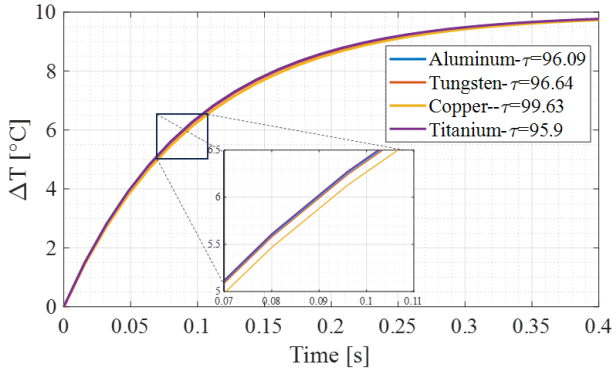

Figure 8. Transient thermal simulation results for different metal selection of the MIM. The thermal time constants in the figure are in milliseconds.

As shown in Figure 8, the choice of metal for the MIM within the TMOS structure had a minimal impact on its thermal performance, consistent with simulation results. The heat capacity equation, coupled with Table 1, indicates that copper has the longest thermal time constant among CMOS-compatible metals due to its high specific heat capacity and density. However, transient simulations revealed that MIM thickness, rather than metal

selection, significantly influenced thermal performance. To further investigate this effect, Figure 9 presents results for TMOS structures with varying MIM insulator thicknesses.

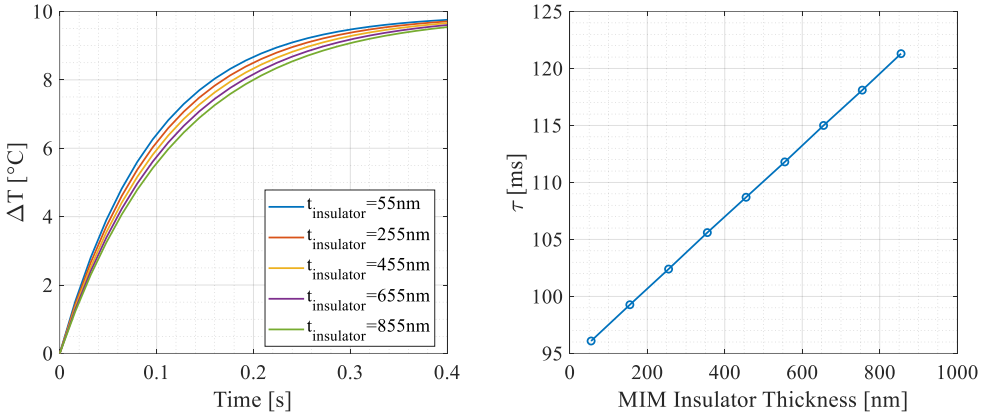

(**a**) (**b**)

Figure 9. Transient simulation results for different MIM insulator thickness: (**a**) The temperature difference of the TMOS pixel as function of the time, for different MIM insulator thickness; (**b**) the calculated thermal time constant versus the MIM insulator thickness.

As depicted in Figure 9, thicker MIM structures exhibit a pronounced increase in thermal time constant, suggesting a delayed thermal response.

Table 2 summarizes the thermal and optical impact of MIM integration with TMOS and CMOS-SOI-MEMS thermal sensors:

Table 2. Summarize of MIM disk with radius of 633 nm in this study on the thermal and optical properties of the TMOS sensor at wavelength of 4.26 μm.

Parameter	Units	Without MIM	With MIM	Impact of MIM Integration	Notes
η—Optical absorption efficiency	N. A	0.77	0.9871	28.19% increasement	Excellent efficiency improvement. And good for sensor selectivity
G_{th}—Thermal conductance	$\frac{W}{K}$	1.0069×10^{-7}	1.0089×10^{-7}	0.2% increasement	practically no effect
τ_{th}—Thermal time constant	ms	86	96.25	12% increasement	Unwanted tradeoff—slower response time
$R_T(\omega = 0) = \frac{\Delta T}{P_{opt}} = \frac{\eta}{G_{th}}$ DC temperature responsivity: temperature difference to optical power ratio	$\frac{K}{W}$	7.65×10^{6}	9.78×10^{6}	27.84% increasement	Since the thermal conductance has small impact the change in responsivity is relative to the change of the optical absorption efficiency

4. Conclusions

This study used FDTD simulations to examine the integration of a metal-insulator-metal (MIM) metamaterial absorber with a CMOS-SOI-MEMS infrared sensor. Results showed near-perfect absorption (>98%) in the mid-infrared region. The MIM disk radius affected the absorption spectrum, with larger radii causing redshift and decreased quality factor. While the MIM structure minimally impacted thermal conductance, it influenced

thermal capacitance and time constant. Transient thermal simulations revealed that larger MIM radii slightly increased thermal time constants. The MIM insulator thickness significantly affected thermal performance, with thicker structures increasing thermal time constants. Metal choice had minimal impact. The study concludes that MIM integration can enhance sensor absorption efficiency, but careful design consideration is necessary to minimize adverse thermal effects.

The MIM structure exhibits exceptional selectivity, making it highly advantageous for NDIR gas sensor applications. Various gases possess distinct resonance frequencies, exemplified by CO_2, which demonstrates an absorption resonance at 4.26 μm, utilized for optical detection in the mid-infrared range. The proposed MIM structure in this study enhances the TMOS absorption efficiency by 20% at this resonance, potentially improving sensor sensitivity.

Furthermore, the MIM's high selectivity facilitates multi-gas detection, as non-combustion gases exhibit unique resonance frequencies. Integration of diverse MIM structures on different pixels within a single device may enables the development of miniaturized NDIR gas sensors. Consequently, the incorporation of metamaterial absorbers, particularly MIM absorbers, on CMOS-SOI thermal sensors demonstrates significant potential. The findings of this study indicate the suitability of this approach for advanced IR and gas sensing applications.

Author Contributions: Conceptualization, M.A. and Y.N.; methodology, M.A. and M.K.; software, M.A. and M.K.; validation, M.A. and M.K.; formal analysis, M.A. and Y.N.; investigation, M.A. and M.K. and Y.N.; resources, M.A. and M.K.; data curation, M.A., M.K. and Y.N.; writing—original draft preparation, M.A.; writing—review and editing, M.A., M.K. and Y.N.; visualization, M.A. and M.K.; supervision, Y.N.; project administration, Y.N.; funding acquisition, Y.N. All authors have read and agreed to the published version of the manuscript.

Funding: This research received no external funding.

Institutional Review Board Statement:

Informed Consent Statement:

Data Availability Statement: the data presented in this study are available on reasonable request from the corresponding author.

Acknowledgments: The authors would like to express their gratitude to their colleagues in Prof. Nemirovsky's group for support and advice and to the VLSI laboratory at the electrical and computer engineering department for providing the necessary infrastructure.

Conflicts of Interest: The authors declare no conflict of interest.

References

1. Balcerak, R.S. Uncooled infrared sensors: Rapid growth and future perspective. In Proceedings of the AeroSense 2000, Orlando, FL, USA, 24–28 April 2000; Dereniak, E.L., Sampson, R.E., Eds., pp. 36–39. https://doi.org/10.1117/12.391763.
2. Moisello, E.; Malcovati, P.; Bonizzoni, E. Thermal Sensors for Contactless Temperature Measurements, Occupancy Detection, and Automatic Operation of Appliances during the COVID-19 Pandemic: A Review. *Micromachines* **2021**, *12*, 148. https://doi.org/10.3390/mi12020148.
3. Saraf, T.; Brouk, I.; Shefi, S.B.-L.; Unikovsky, A.; Blank, T.; Radhakrishnan, P.K.; Nemirovsky, Y. CMOS-SOI-MEMS Uncooled Infrared Security Sensor with Integrated Readout. *IEEE J. Electron Devices Soc.* **2016**, *4*, 155–162. https://doi.org/10.1109/JEDS.2016.2539980.
4. Wei, J.; Ren, Z.; Lee, C. Metamaterial technologies for miniaturized infrared spectroscopy: Light sources, sensors, filters, detectors, and integration. *J. Appl. Phys.* **2020**, *128*, 240901. https://doi.org/10.1063/5.0033056.
5. Lochbaum, A.; Dorodnyy, A.; Koch, U.; Koepfli, S.M.; Volk, S.; Fedoryshyn, Y.M.; Wood, V.; Leuthold, J. Compact Mid-Infrared Gas Sensing Enabled by an All-Metamaterial Design. *Nano Lett.* **2020**, *20*, 4169–4176. https://doi.org/10.1021/acs.nanolett.0c00483.
6. Sharma, A.; Singh, H.; Gupta, A. A Review Analysis of Metamaterial-Based Absorbers and Their Applications. *J. Supercond.* **2022**, *35*, 3067–3083. https://doi.org/10.1007/s10948-022-06394-3.
7. Glybovski, S.B.; Tretyakov, S.A.; Belov, P.A.; Kivshar, Y.S.; Simovski, C.R. Metasurfaces: From microwaves to visible. *Phys. Rep.* **2016**, *634*, 1–72. https://doi.org/10.1016/j.physrep.2016.04.004.

8. Urquia, M.A.; Allegato, G.; Paleari, S.; Tripodi, F.; Oggioni, L.; Garavaglia, M.; Nemirovsky, Y.; Blank, T. High vacuum wafer level packaging for uncooled infrared sensor. In Proceedings of the 2020 Symposium on Design, Test, Integration & Packaging of MEMS and MOEMS (DTIP), Lyon, France, 15–26 June 2020; IEEE: Piscataway, NJ, USA, 2020; pp. 1–5. https://doi.org/10.1109/DTIP51112.2020.9139148.
9. Avraham, M.; Golan, G.; Vaiana, M.; Bruno, G.; Castagna, M.E.; Stolyarova, S.; Blank, T.; Nemirovsky, Y. Wafer-Level Packaged CMOS-SOI-MEMS Thermal Sensor at Wide Pressure Range for IoT Applications. *Eng. Proc.* **2020**, *2*, 30. https://doi.org/10.3390/ecsa-7-08191.
10. Dorodnyy, A.; Koepfli, S.M.; Lochbaum, A.; Leuthold, J. Design of CMOS-compatible metal–insulator–metal metasurfaces via extended equivalent-circuit analysis. *Sci. Rep.* **2020**, *10*, 17941. https://doi.org/10.1038/s41598-020-74849-5.
11. Ansys Lumerical. Available online: https://www.lumerical.com (accessed on August 2024).
12. Avraham, M.; Stolyarova, S.; Blank, T.; Bar-Lev, S.; Golan, G.; Nemirovsky, Y. A Novel Miniature and Selective CMOS Gas Sensor for Gas Mixture Analysis—Part 2: Emphasis on Physical Aspects. *Micromachines* **2020**, *11*, 587. *https://doi.org/*10.3390/mi11060587.
13. Ansys Mechanical. Available online: https://www.ansys.com/products/structures/ansys-mechanical (accessed on August 2024).